Energy Engineering

Tech Science Press

Doi:10.32604/ee.2026.075468

ARTICLE

Check for updates

Engineering Application of Numerical Calibration of Wind Power in Complex Terrain Wind Farms

Xin Guan[1,*], Dechen Kong[1], Hao Tang[1], Bo Liu[1] and Chuang Zhao[2]

[1]School of Energy and Power Engineering, Shenyang Institute of Engineering, Shenyang, 110136, China
[2]Guoneng (Suizhong) Power Generation Co., Ltd., Huludao, 125222, China

*Corresponding Author: Xin Guan. Email: xin_guan@sina.com

Received: 01 November 2025; Accepted: 05 January 2026; Published: 30 August 2026

ABSTRACT: Numerical calibration of wind power is a critical strategy for mitigating power generation deficits and optimizing the micro-siting of wind turbine units. As wind energy development shifts towards mountainous regions, accurate assessment in these environments becomes increasingly challenging due to complex turbulence structures. This paper conducts a theoretical and numerical investigation of atmospheric boundary layer flow in complex terrain. Utilizing the industry-standard Askervein Hill benchmark for validation, we first evaluate the influence of top boundary condition settings in rectangular fluid domains on the simulation accuracy of the equilibrium atmospheric boundary layer. Subsequently, the study proposes a method to optimize the coefficients of the k-ε turbulence model. By designing nonlinear orthogonal experiments, the range of turbulence parameters is refined, and the spatial discretization error is systematically analyzed to minimize the deviation in turbulent kinetic energy. The results demonstrate that the optimized turbulence model coefficients significantly improve the stability and accuracy of wind power density calibration. Specifically, the proposed methodology effectively reduces the high prediction errors typically observed in the leeward wake regions of mountains. Additionally, a hybrid grid strategy—combining unstructured grids near the terrain surface with structured grids elsewhere—is recommended to balance computational efficiency and accuracy. This study provides a robust engineering reference for wind resource assessment in complex topographical conditions.

KEYWORDS: Numerical calculation; wind power calibration; reliability; k-ε; fluent

1 Introduction

Wind resource assessment is the foundational step in the development of wind power projects. Its primary objective is to accurately quantify, analyze, and evaluate the density, distribution, and availability of wind energy resources within a target region. With the refined advancement of the wind power market, the exploitation of wind resources has progressively shifted from flat terrain—characterized by stable wind and favorable construction conditions—to complex mountainous environments. These regions, however, present challenges such as high turbulence and significant construction difficulties. Furthermore, the assessment process is often hindered by a lack of high-resolution terrain data, leading to compromised assessment accuracy. Computational Fluid Dynamics (CFD) technology offers a solution by simulating flow fields over complex topographies, such as mountainous and hilly regions, while explicitly accounting for the aerodynamic effects of terrain undulations and obstacles to accurately predict wind speed and direction. Consequently, conducting a reliability analysis of existing numerical calculation methods for complex terrain and developing an automated platform based on these optimized processes holds substantial research value and engineering significance [1–5]. Recent studies have highlighted that uncertainty in wind resource assessment remains a critical challenge, particularly regarding error distribution in leeward wake regions and flow separation zones [6–8].

The application of CFD technology in numerical calculations of wind engineering is called "computational wind engineering". Zou et al. [9] investigated the wind field characteristics of complex terrain based on experimental and numerical methods, and Yoon [10] simulated the temporal characteristics of three-dimensional turbulence over rough surfaces through DNS. At present, most of the numerical models used for evaluating wind resources are CFD models. Song et al. [11] utilized elevation data to reconstruct complex mountainous terrains and conducted numerical simulations of wind flow parameters. Moreover, CFD can depict the details of turbulent flow under the influence of terrain and performs better than linear models in the assessment of wind resources in complex terrains. To further make the CFD model meet the requirements of actual wind field flow, the researchers first studied the equilibrium atmospheric boundary layer that needs to be considered most. Ayuso-Virgili et al. [12] evaluated the performance of four measure-correlate-predict models for improving wind energy assessment accuracy. Shen et al. [13] developed an equilibrium atmospheric boundary layer (EABL) model to improve the accuracy of wind field simulations.

To address the urgent need for the transformation of wind energy development and utilization from flat terrain to complex terrain, and also to provide a complete database for verifying CFD models, multiple field wind measurement experiments have been carried out internationally. Recent studies by Ma et al. [14] have evaluated the performance of RANS turbulence models for predicting wind flow characteristics over typical complex terrains. Building on this, Bretos et al. [15] conducted an in-depth analysis of wind farm flow and wake characteristics in complex terrain by combining numerical simulations with experimental measurements.

2 Theoretical Analysis

2.1 Characteristics of Atmospheric Boundary Layer Flow

The atmospheric boundary layer is the lowest layer of the troposphere in the Earth's atmosphere and is directly influenced by factors such as surface friction, terrain undulations and vegetation. The flow characteristics of the atmospheric boundary layer are mainly manifested as vertical variations in wind speed and turbulent structures [16]. These characteristics determine the interaction between the surface and the atmosphere and affect the practical application of wind resource assessment. Under the cushion surface of the atmospheric boundary layer (that is, the part below the free atmosphere), at the height where the wind turbine is located, the energy of turbulence comes from mechanical work and buoyancy work. In the atmospheric boundary layer of stable stratification, turbulence is usually weak or completely absent, but there is a strong wind shear between the upper and lower layers, which will generate shear gravity waves. When the shear is large enough, the density is inverted, the amplitude of wave motion increases and breaks, and the broken waves superimpose to form turbulence. The formation of turbulence intensifies the mixing of the upper and lower layer flows, thereby weakening wind shear.The motion gradually returns to a state without turbulence, thus repeating this cycle. Recent observations confirm that turbulence generated by Kelvin-Helmholtz waves is highly discrete in space (manifesting as tubes and knots) and intermittent in time [17].

The main feature of the equilibrium atmospheric boundary layer is that the thermodynamic and dynamic processes of the atmosphere are in a stable or quasi-stable equilibrium state, and the wind speed profile is relatively stable, conforming to the commonly used logarithmic law distribution. The stability of the equilibrium atmospheric boundary layer simplifies the CFD simulation process relatively, especially when calculating wind speed distribution and turbulence intensity, reducing the complexity of the model.

Under complex terrain conditions, the equilibrium state assumption, as the preliminary setting for numerical calculation, can highly restore the atmospheric flow characteristics of flat terrain, thereby improving the numerical calculation accuracy of complex terrain conditions, as shown in Fig. 1.

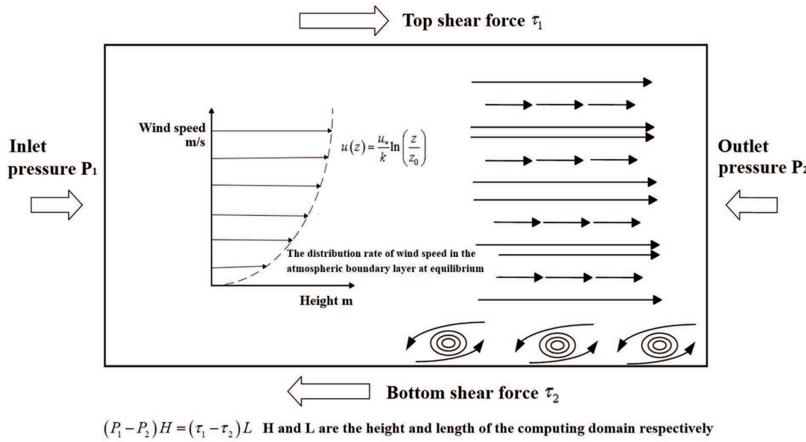

Figure 1: Schematic diagram of atmospheric boundary layer flow in equilibrium state

2.2 Classification of Wind Farm Terrain

Measurement experiments show that when the windward slope is greater than 22° and the leeward slope is greater than 17°, the flow shedding phenomenon will occur [18]. Therefore, in the industry, a slope greater than 30° is usually regarded as the dividing line between simple terrain and complex terrain. Based on the boundary line rules and the geomorphic features of the terrain, the terrain has been further classified. Currently, there are mainly four types of terrain, namely flat terrain, simple mountain terrain, complex mountain terrain, and special complex mountain terrain, as shown in Fig. 2.

3 Numerical Verification of Wind Farms in Complex Terrain

The method for setting the optimal boundary conditions of the equilibrium atmospheric boundary layer was applied to the numerical simulation of actual wind farms. CFD numerical calculations were conducted on the actual wind measurement project ASKERVEIN Mountain. The calculation results were quantitatively compared and analyzed with the measured wind speed to verify the reliability of the k-ε turbulence model in the assessment of wind resources in complex terrain.

3.1 ASKERVEIN Mountain Wind Measurement Project

In order to provide certain data support for the numerical simulation of wind resource assessment under complex mountain conditions, the wind resources research institution conducted a series of field wind measurement experiments on ASKERVEIN Mountain on the west coast of South Euygett Island in the Southern Hebrides of Scotland from September to October 1983. Fig. 3 shows the satellite location of the mountain. The mountain is 116 m high and almost elliptical in shape (with a long axis of approximately 2000 m and a short axis of about 1000 m). The mountain is relatively gentle with a lower slope. The terrain in the southwest is flat, while that in the northeast is more complex. At present, both the surveying and mapping data and the wind measurement data of this project are fully disclosed. The experimental data studied in this paper adopts the TU03-B data from the ASKERVEIN Mountain wind measurement project (wind speed data on 03 October 1983) [19].

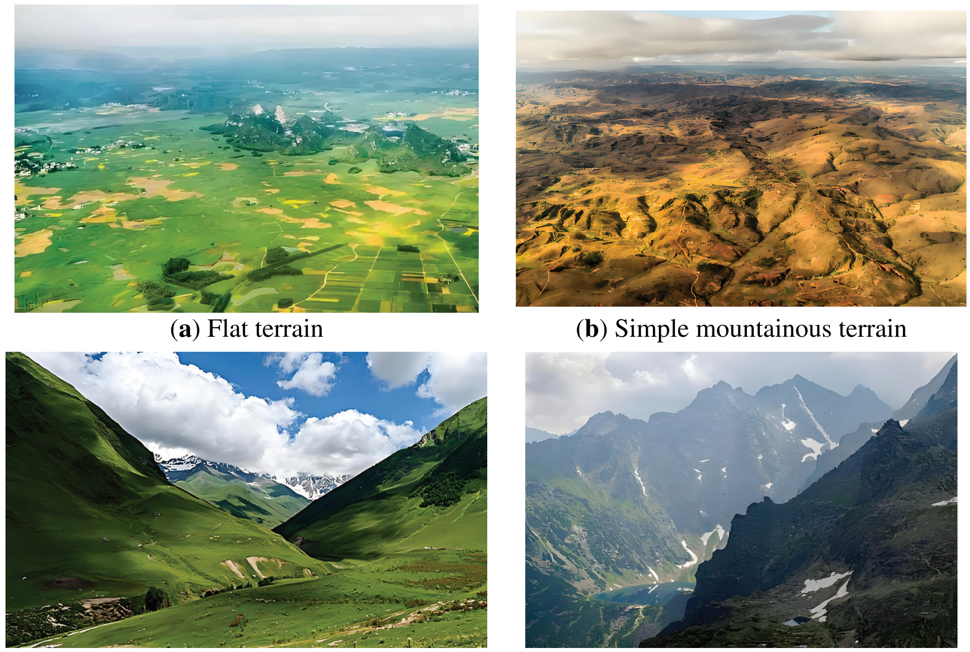

(**a**) Flat terrain (**b**) Simple mountainous terrain

(**c**) Complex mountain terrain (**d**) Special complex mountain terrain

Figure 2: Classification of wind farm terrain

Figure 3: ASKERVEIN satellite location map

The ASKERVEIN mountain wind measurement project has installed a total of 50 wind measurement towers, evenly distributed at height of 10 m above the ground along the A-A, AA-AA, and B-B lines of the mountain. The intersection point of the B-B and A-A lines is the highest point HT of the mountain, with an altitude of 126 m. The intersection points of the B-B line and the AA-AA line are the second-highest point CP of the mountain, with an altitude of 116 m. Point RS is an independent wind measurement point outside the mountain, located 3000 m southwest of point HT. The distribution positions of the wind measurement towers on the mountain and the distribution positions of each characteristic point are shown in Fig. 4.

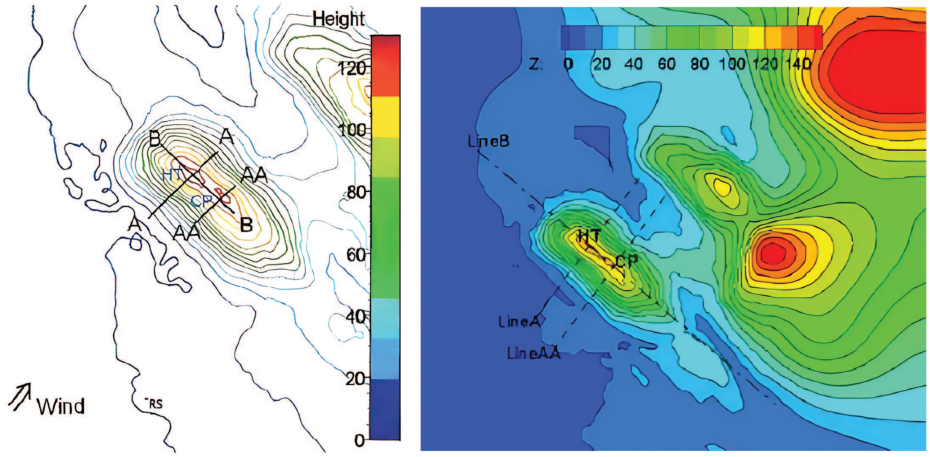

Figure 4: Satellite contour map of the ASKERVEIN mountains

3.2 ASKERVEIN Mountain Geometry Modeling

The physical mountain modeling software in this paper adopts CATIA parametric modeling. Based mainly on the published mapping data [20], combined with the ARCGIS satellite elevation map, the local area is downloaded using the Global Mapper software. The elevation file was in DEM format and exported in *.xyz format. The elevation coordinates were extracted by interpolation in combination with the surveying and mapping data. The extracted mountain coordinate parameters are shown in Table 1.

Table 1: Extraction table of 3D coordinates of mountains

X	*Y*	*Z*
−102.07658	0	112.81997
0	1486.41057	−2.17414
411.94204	200.04875	−52.38479
...	...	...
1001.54274	450	−11.39956
1001.15304	450	−7.94825
1000.76333	450	−4.11347

Based on the mountain point cloud coordinate data in Table 1, a 1:1 model of the ASKERVEIN mountain was conducted with the parametric modeling function of CATIA. Set the highest point HT of the mountain altitude as the origin of the coordinate system (the intersection of the B-B line and the A-A line). The fluid flow direction of the entire basin of the model is east-west, and the mountain model is distributed from north to south. The numerical calculation of the mountain model is shown in Fig. 5.

Fig. 6 shows the contour line graph of the mountain geometric modeling. From the values in the figure, it can be seen that the highest point HT in the mountain geometric modeling is 126.7 m above sea level, with an error of 0.56% compared to the actual altitude of 126 m. The second highest point CP is 111.7 m above sea level, with an error of 3.7% compared to the actual altitude of 116 m. It can be seen that the numerical calculation model has relatively precise modeling accuracy at the mountain top.

Figure 5: Geometrical modelling of the ASKERVEIN hill

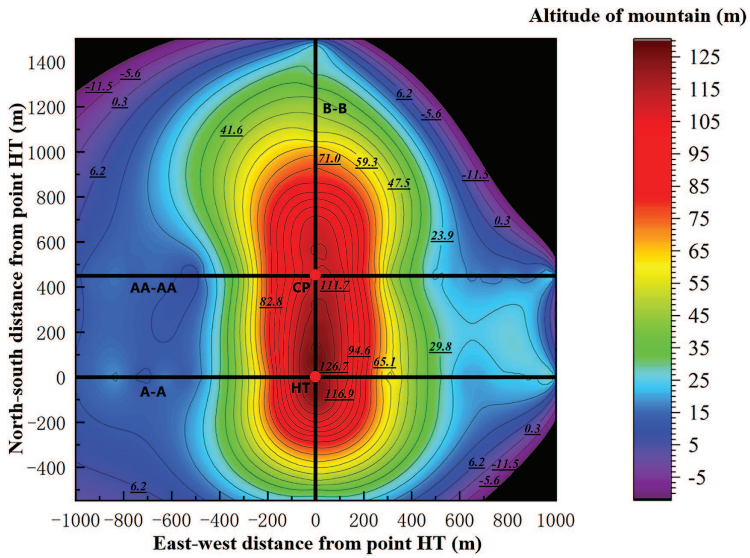

Figure 6: Contour map for geometric modelling of ASKERVEIN mountains

3.3 Calculation Settings and Boundary Condition Settings

The details of grid division and fluid flow direction are shown in Fig. 7. Taking the highest point of the mountain, HT, as the coordinate origin, it extends 5000 m in the north-south direction (Y-axis direction) and 6000 m in the east-west direction (X-axis direction). The height of the basin (Z-axis) is 1200 m. The calculation grid adopts a structural grid, and the total number of grids is 3.5×10^7.While hybrid grid strategies are often recommended for balancing surface stability [21], this study utilizes a high-resolution structural grid validated for spatial discretization accuracy using methods similar to Richardson extrapolation [22]. The details of grid division and fluid flow direction are shown in Fig. 7.

The numerical calculation was carried out using the FLUENT solver. The ground was a non-slip solid wall boundary. The outlet boundary was set at the local meteorological data given atmospheric pressure of 1.013×10^5 Pa, and the wind speed direction was orthogonal to the inlet cross-section. The inlet wind speed, turbulent kinetic energy and its dissipation are all given by the UDF and satisfy the function distribution constraints as shown in Eqs. (1)–(3) below. The selection of these top and inlet boundary conditions is critical for maintaining the equilibrium of the atmospheric boundary layer, as confirmed by recent validation studies [23].

$$u = \frac{u^*}{K} \ln\left(\frac{z - z_1}{z_0}\right) \tag{1}$$

$$K = \begin{cases} \frac{u^{*2}}{\sqrt{C_\mu}}\left[1 - \frac{z-z_1}{h_g}\right]^2 & z \le z_1 + h_g \\ 0 & z > z_1 + h_g \end{cases} \tag{2}$$

$$\varepsilon = \frac{u^{*3}}{K\left(z - z_1\right)} \tag{3}$$

In the formula, K is von Karman constant is taken as 0.4, z_1 represents the altitude of the inlet boundary, u^* is the friction velocity, z_0 is the roughness height taken as 0.03 m from the mapping data, and h_g is the thickness of the atmospheric boundary layer, which is calculated to be h_g = 909.56 m based on the local longitude and latitude. From Eqs. (1)–(3), it can be seen that the frictional velocity is directly related to the velocity distribution at the inlet, the distribution of turbulent kinetic energy, and the distribution of turbulent kinetic energy dissipation. Therefore, in order to accurately provide the expressions of the inlet and outlet velocities, turbulent kinetic energy, and their dissipation, the accuracy of the value of the frictional velocity needs to be improved. Most researchers conduct simulation calculations for complex terrain wind fields based on the wind speed data at fixed height in certain wind measurement point. They substitute the fixed-height wind measurement data at one point into the constraint function to solve the friction velocity u^* with undetermined coefficients. The friction velocity or distribution solved by this prior method only meets 100% accuracy at a fixed height, while the corresponding distribution errors at other positions are relatively large. The multi-point wind measurement data at different elevations are adopted for function fitting to ensure that the overall distribution has high accuracy, and then the value of the friction velocity is determined by the function. Based on this method combined with the function expression structure, the wind speed inlet distribution function as shown in Fig. 8 was obtained by fitting the wind measurement data at different elevations of the on-site measured point RS (Table 2) with a custom function. It can be seen that the correlation coefficient accuracy between the fitted speed inlet wind speed function distribution and the measured wind speed at different heights reaches 99.4%, which can be used to solve the friction velocity of the mathematical model. Therefore, by fitting the expression of the wind speed function, the friction velocity can be calculated as 0.6117 (m/s). It should be particularly noted that its turbulent kinetic energy satisfies a functional distribution when the height is less than or equal to the atmospheric boundary layer. When the height is greater than the height of the atmospheric boundary layer, the actual observed turbulent kinetic energy approaches 0. Therefore, processing is done as 0 here, and the turbulent kinetic energy dissipation setting satisfies Eq. (3).

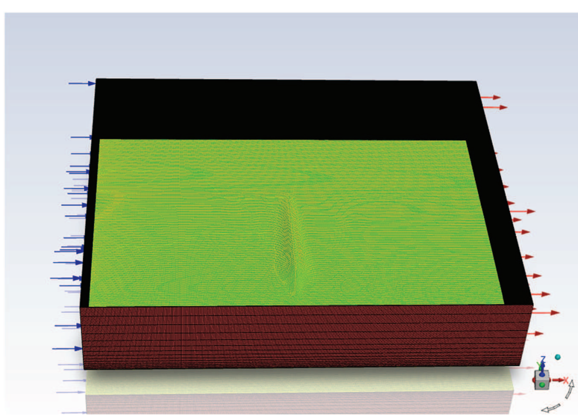

Figure 7: Schematic diagram of the computational domain of a mountain body

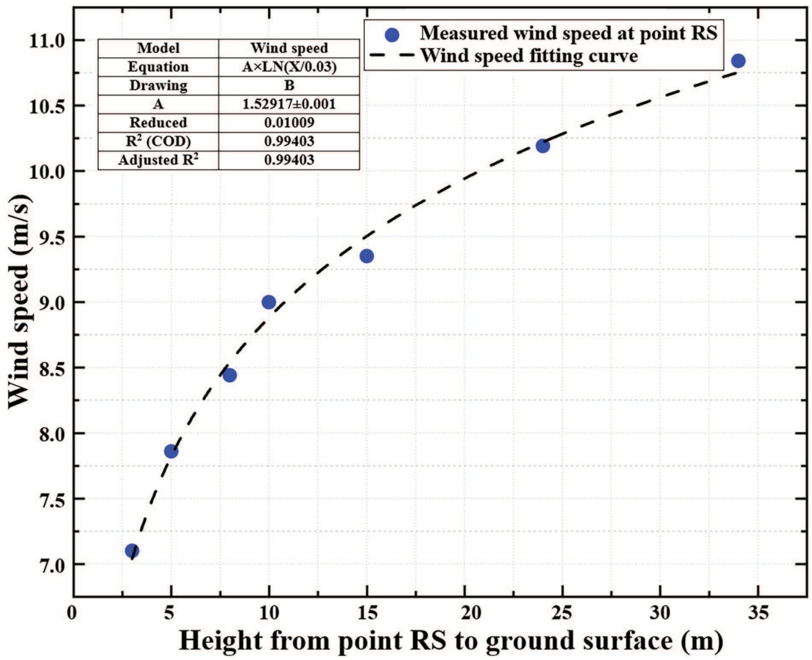

Figure 8: Plot of measured wind speed fitting inlet wind speed function

Table 2: Mountain field wind measurement data sheet

Wind Speed (m/s)		
Height (m)	**RS**	**HT**
3	7.1	15.71
5	7.86	16.38
8	8.44	16.3
10	9	16.2
15	9.35	16.63
24	10.19	16.15
34	10.84	15.77

To ensure the calculation accuracy, the RNAS algorithm is selected for the solution algorithm, and the turbulence model is a two-way k-ε turbulence model. The turbulence model is modified to $C_{1\varepsilon} = 1.21$; $C_{2\varepsilon} = 1.92$; $C_\mu = 0.03$; $\sigma_k = 1.0$; $\sigma_\varepsilon = 1.3$. The calculation is set to be based on the pressure-velocity coupled SIMPIEC method. The spatial discrete format adopts the second-order upwind mode, and the residual convergence degree is set to 10^{-3}. The turbulent kinetic energy at the outlet is used as the monitoring quantity for calculation and monitoring to ensure that the turbulent kinetic energy is fully developed and advanced to the outlet for solution calculation.

3.4 Simulation Analysis

The mountain is affected by the altitude gradient. Generally, the wind speed is higher at the top of the mountain, while it is significantly weakened on the leeward side. Fig. 9 shows the static pressure map of the mountain surface. It can be seen from the figure that the pressure on the windward side of the mountain is greater than that in other areas, while the relative pressure at the ridge is negative. The pressure on the leeward side is smaller than that on the windward side but greater than that at the ridge. This causes the fluid on the windward side to rapidly squeeze towards the ridge of the negative pressure area, resulting in a rapid increase in wind speed at the ridge or the mountain top. Although the pressure on the leeward side is slightly lower than that on the windward side, the cross-section behind the mountain is correspondingly expanded and there is a fluid bypass phenomenon, so the flow velocity is smaller than the wind speed on the windward side.

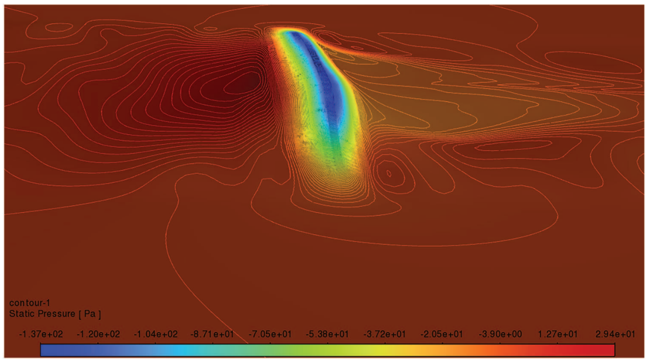

Figure 9: Contour plot of static pressure on the mountain surface

As shown in Fig. 10a, it can be seen that the maximum CFD calculated wind speed of the wind field is 15.3 m/s, and its maximum wind speed is located at the ridge or the top of the mountain. This further confirms the conclusion of the static pressure analysis that the wind speed on the leeward side is significantly smaller, indicating that the wind speed is blocked by the mountain. Due to the fluid flow around, the wind speed is significantly reduced on the leeward side. From the density of the velocity contour lines in the figure, it can be seen that the contour lines at the mountain top are relatively dense, indicating that the ridge is a high-wind-speed area. Although the wind speed on the windward side is also relatively high, the distance between the wind speed contour lines is too scattered, indicating that the wind speed distribution gradient is small. On the leeward side of the mountain, the wind speed is more variable due to the increase in turbulence. From the wind speed cloud maps at various heights in the comprehensive Fig. 10, it can be seen that as the height increases, the density of the contour lines gradually decreases. From this, it can be analyzed that the effect of the fluid on the windward side squeezing towards the ridge gradually weakens as the height increases. The wind speed at the top of the mountain gradually stabilizes. For the fluid on the leeward side, the turbulence degree also gradually weakens as the height increases. After reaching a certain height, the influence of the mountain terrain on the fluid disappears and tends to be laminar flow.

Due to the fact that ASKERVEIN Mountain is constantly hit by southwest winds, which are almost parallel to the A-A line and AA-AA line of the mountain, and the wind measurement towers of the project are evenly distributed along the A-A line and AA-AA line, almost orthogonal to the measured wind, etc. Therefore, by comparing and analyzing the simulated wind speed data of the mountain section along the A-A line and the mountain section along the AA-AA line with the measured data, not only can the error analysis of the calculation results of the numerical algorithm adopted in this paper be further conducted, but also the interference of wind direction on the wind speed simulation can be effectively ignored, making it more of engineering significance. As shown in Fig. 11a, the wind speed at the A-A mountain section follows A logarithmic rate distribution along height, which is consistent with the experimental observations. Moreover, the highest wind speed point is the highest altitude point HT, with A wind speed of 15.3 (m/s). Combining the measured wind speed data, it can be inferred that the simulation error of the wind speed at this point is 2.6%. Here, it is assumed that the experimental error is 0. For the same reason, as shown in Fig. 11b, the error estimation of the second-highest point CP of the mountain altitude on the AA-AA line was conducted, and the simulation error of this point was obtained to be 4.9%. Therefore, it can be seen that the simulated wind speed has high accuracy at the summit.

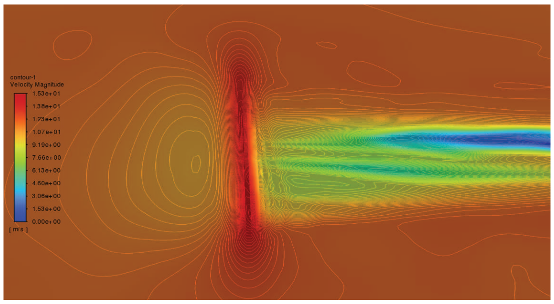

(**a**) 3 m above the ground

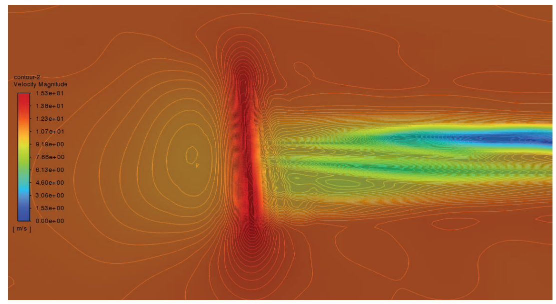

(**b**) 5 m above the ground

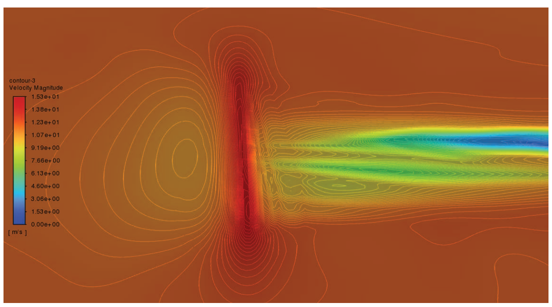

(**c**) 8 m above the ground

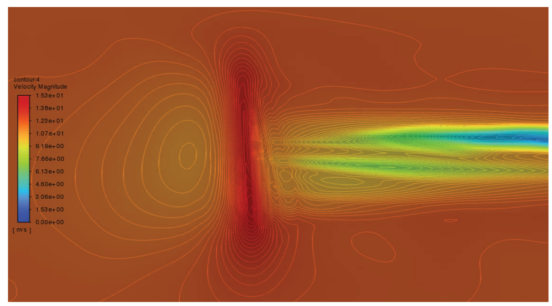

(**d**) 10 m above the ground

Figure 10: Wind speed cloud at different elevations of the mountain

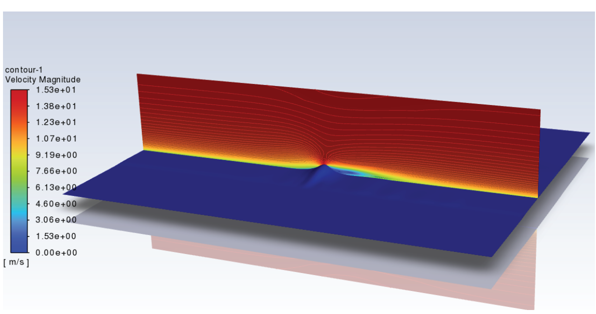

(**a**) A-A cross-section

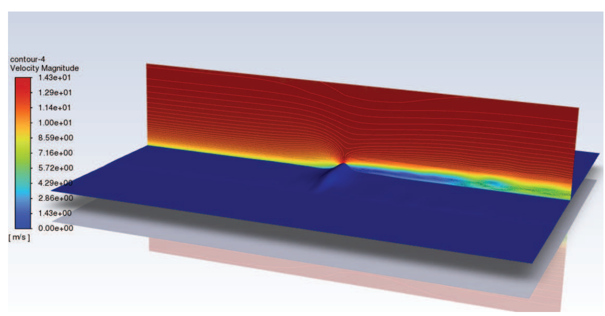

(**b**) AA-AA cross-section

Figure 11: Wind speed cloud map

To assess the calculation error of the simulated wind speed as comprehensively as possible, the distribution positions of the wind measurement towers along the A-A line and AA-AA line [24] were selected as feature points to conduct multi-point comparisons between the simulated wind speed and the measured wind speed, and the comparison results in Fig. 12a,b was obtained. It is found from the error calculation of multiple feature points that the simulated wind speed errors of each point on the A-A line and the AA-AA line can be maintained within 8%, and the wind speed variation trend is basically consistent with the change of mountain altitude, which is in line with the overall trend of the actual observation and experimental results.

Therefore, it can be seen that this numerical calculation model has high reliability and can be used for the mutual deduction of wind speed in actual wind engineering calculations.

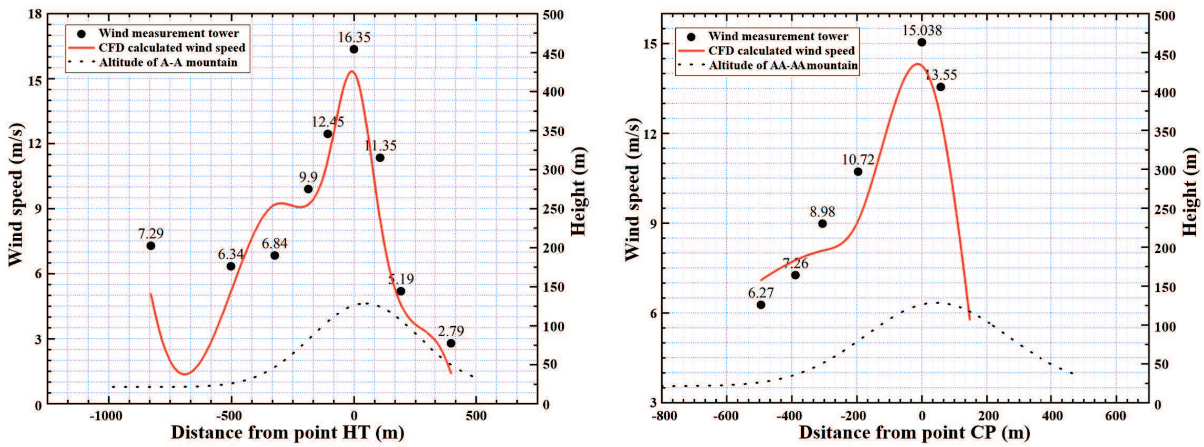

(**a**) Lines A-A (**b**) AA-AA line

Figure 12: Wind speed comparison chart

4 Reliability Analysis of Turbulence Model Parameters

From the previous research and analysis, it can be known that under complex terrain conditions, the simulation error of wind speed is greatly affected by turbulence parameters. In the later stage of wind resource assessment work, it is necessary to correct the calibration error of the wind power curve, which requires the simulation calculation results to maintain a relatively small average error. Therefore, with the aim of reducing the simulation error of wind speed and the fluctuation of its error, the parameters of the turbulence model were optimized and analyzed under complex terrain conditions, and the optimal coefficient under this condition was obtained.

4.1 Reliability Selection of Turbulence Parameters

Under numerical calculation, to optimize the reliability of turbulence parameters, it is necessary to define the range of turbulence parameter values that are relatively reliable for numerical calculation based on complex terrain conditions. Turbulent kinetic energy introduces the most significant uncertainty in flow field calculations.Sensitivity analyses indicate that standard turbulence model parameters often lead to prediction deviations in complex terrain, necessitating specific coefficient corrections [25,26]. It is observed that the errors in wind speed and turbulent kinetic energy dissipation are strongly correlated with the turbulent kinetic energy error. Therefore, to minimize calculation deviation and enhance stability, the standard deviation of the turbulent kinetic energy error is selected as the primary objective function for optimization. Therefore, in order to further reduce the calculation error and improve the stability of the error, the standard deviation of the turbulent kinetic energy error should be taken as the basis for correction.

In numerical calculations, turbulent kinetic energy is expressed as

$$k = \frac{3}{2}(UI)^2 \tag{4}$$

In the formula, k is turbulent kinetic energy, with the unit of (m^2/s^2); $I = \frac{\sqrt{(u^2+v^2+w^2)/3}}{U}$ is the turbulence intensity, and u, v, and w are respectively the three-dimensional pulsating wind speed components, with the unit of (m/s). U is the average wind speed, measured in (m/s).

To ensure the engineering accuracy of the selection range of turbulent kinetic energy, the physical locations of the characteristic points are in accordance with the "Wind Energy Measurement Method for Wind Farms" specification. The turbulent kinetic energy measurement data of the ASKERVEIN Mountain A-A line at height of 10 m above the ground are shown in Table 3. By adjusting the parameters of the turbulence model for calculation, it was found that the lowest simulated average error of the turbulent kinetic energy at the selected feature points was 9.23%. Therefore, taking the turbulent kinetic energy error less than 9.23% as the division standard, the value range of the turbulence model coefficients was divided. The obtained turbulence model coefficient values were C_μ within the range of [0.03, 0.09]. σ_k is within the range of [0.3, 1.3], σ_ε is within the range of [0.6, 1.6], $C_{1\varepsilon}$ is within the range of [1, 1.6], $C_{2\varepsilon}$ is between [1.65, 2.25].

Table 3: Measurement of turbulent kinetic energy on line A-A of ASKERVEIN Hill at 10 m above ground level

The distance from point HT m	Average wind speed m/s	Turbulence intensity *u*	Turbulence intensity *v*	Turbulence intensity *w*	Turbulent kinetic energy m^2/s^2
−350	7.2	0.174	0.145	0.081	0.028931
−200	10.5	0.107	0.107	0.054	0.012907
−100	13.2	0.080	0.093	0.044	0.0084925
HT	16.2	0.068	0.064	0.036	0.005008
100	12.0	0.146	0.084	0.044	0.015154
200	5.6	0.458	0.269	0.158	0.15354
400	3.0	0.668	0.606	0.402	0.487532

4.2 Optimization and Correction of Turbulence Parameters

As can be seen from the above text, during the process of dividing the reliability range of turbulence parameters, the minimum error turbulence parameter setting range under the same numerical calculation conditions has been found. To further enhance the error stability of the numerical calculation results, this section will, within the selected turbulence model parameter range, continuously reduce the average error standard deviation of the turbulent kinetic energy of the characteristic points to improve the error stability of its numerical calculation. When the standard deviation of the simulation error of the turbulent kinetic energy at the characteristic point is the smallest, it can be regarded as the turbulence parameters have been optimized and corrected, and this turbulence coefficient can be used for the mutual deduction of wind speed in actual engineering calculations. According to the three-dimensional expression of the turbulence model in the previous text, it can be seen that the influence of turbulence parameters on numerical calculation is nonlinear. Therefore, in the process of turbulence parameter optimization, the influence of a single parameter cannot be considered only, but rather the combination of various parameters is needed to find the optimal solution.This optimization strategy aligns with recent findings aimed at enhancing CFD simulation accuracy through algorithm-based parameter tuning [27]. Therefore, five values were uniformly selected within the parameter range, as shown in Table 4. The turbulence parameters were optimized and corrected based on the 5-factor 5-level values formed in Table 5. A preliminary orthogonal experiment was conducted under the ASKERVEIN mountain condition. The new value range was further divided from the error analysis, and multiple rounds of orthogonal experiment calculations were carried out until the standard deviation no longer decreased further, thereby completing the optimization and correction of the turbulence parameters. The orthogonal experiment values are shown in Table 5.

Table 4: Table of parameter values

Horizontal value	C_μ	σ_k	σ_ε	$C_{1\varepsilon}$	$C_{2\varepsilon}$
1	0.09	1.3	1.6	1.6	2.25
2	0.075	1.05	1.35	1.45	2.10
3	0.06	0.80	1.10	1.30	1.95
4	0.045	0.55	0.85	1.15	1.80
5	0.03	0.3	0.6	1.0	1.65

Table 5: L_{25} (5^5) Orthogonal table

No.	C_μ	σ_k	σ_ε	$C_{1\varepsilon}$	$C_{2\varepsilon}$	Standard deviation of turbulent kinetic energy error
1	1	1	1	1	1	0.04669
2	1	2	3	4	5	0.04514
3	1	3	5	2	4	0.04513
4	1	4	2	5	3	0.06511
5	1	5	4	3	2	0.05504
6	2	1	5	4	3	0.05512
7	2	2	2	2	2	0.03512
8	2	3	4	5	1	0.03510
9	2	4	1	3	5	0.03507
10	2	5	3	1	4	0.06501
11	3	1	4	2	5	0.03508
12	3	2	1	5	4	0.03507
13	3	3	3	3	3	0.04506
14	3	4	5	1	2	0.06503
15	3	5	2	4	1	0.05496
16	4	1	3	5	2	0.04504
17	4	2	5	3	1	0.03503
18	4	3	2	1	5	0.03502
19	4	4	4	4	4	0.02498
20	4	5	1	2	3	0.05490
21	5	1	2	3	4	0.02515
22	5	2	4	1	3	0.03496
23	5	3	1	4	2	0.02494
24	5	4	3	2	1	0.02490
25	5	5	5	5	5	0.02482

As can be seen from Table 5, the standard deviation of some parameter combinations is relatively large. Therefore, new value ranges are divided based on the corresponding combinations with smaller standard deviations, and orthogonal experiments are conducted. By the third round of calculation, it was found that the standard deviation no longer decreased further, and the final corrected turbulence coefficient was obtained as $C_\mu = 0.03$; $C_{\varepsilon 1} = 1.10$; $C_{\varepsilon 2} = 2.15$; $\sigma_k = 0.85$; $\sigma_\varepsilon = 0.90$.

4.3 Comparative Analysis of Wind Power Calibration

Wind power calibration plays an irreplaceable role in wind resource assessment. It not only provides quantified wind energy resource indicators to guide the site selection of wind farms and the selection and layout of wind turbine generators, but also enhances the accuracy and reliability of wind resource assessment, supporting the planning and operation of wind power projects. Therefore, during the development of wind power projects, great importance should be attached to the calibration of wind power to ensure the reliability of its assessment results.

Wind power refers to the energy that the airflow possesses when passing through a certain cross-sectional area at a certain speed within a unit of time. It can also be understood as the power captured by the wind turbine from the wind and converted into useful work. The magnitude of wind power is closely related to factors such as wind speed, air density, and the capture efficiency of wind turbines. Taking the feature points selected in Fig. 4 as an example, numerical calculations were carried out using different turbulence model coefficients (the coefficient values are shown in Table 6. Referring to the specification "Numerical Field Calibration Method for Power Performance Testing of Wind Turbine Generators in Wind Power Generation Systems", the numerical calculation results at different elevations were selected for the analysis of wind power density calibration errors to verify the actual effect of the optimized and corrected turbulence parameters.

Table 6: Table of values for k-ε turbulence model parameters

Turbulence parameters	C_μ	σ_k	σ_ε	$C_{1\varepsilon}$	$C_{2\varepsilon}$
Default coefficient	0.09	1.0	1.3	1.44	1.92
Literature coefficient	0.03	1.0	1.3	1.21	1.92
The coefficient of this article	0.03	0.85	0.90	1.10	2.15

It can be seen from Fig. 13a,b that at the wind measurement points a and a_1 in front of the mountain, under the default turbulence coefficient, the maximum wind power density error is approximately 55% at distance of 3 m from the mountain surface, and the minimum wind power density error is approximately 30% at distance of 34 m from the mountain surface. Under the turbulence coefficient in the literature, the maximum wind power density error is approximately 48% at distance of 3 m from the mountain surface, and the minimum wind power density error is approximately 22% at distance of 34 m from the mountain surface. Under the corrected turbulence coefficient in this paper, the maximum wind power density error is approximately 29% at distance of 3 m from the mountain surface, and the minimum wind power density error is approximately 20% at distance of 34 m from the mountain surface. It can be seen from Fig. 13c,d that at the wind measurement points b and b_1 on the mountain top, under the default turbulence coefficient, the maximum wind power density error is approximately 48% at distance of 3 m from the mountain surface, and the minimum wind power density error is approximately 35% at distance of 34 m from the mountain surface. Under the turbulence coefficient in the literature, the maximum wind power density error is approximately 44% at distance of 3 m from the mountain surface, and the minimum wind power density error is approximately 29% at distance of 34 m from the mountain surface. Under the corrected turbulence coefficient in this paper, the maximum wind power density error is approximately 30% at distance of 3 m from the mountain surface, and the minimum wind power density error is approximately 20% at distance of 34 m from the mountain surface. It can be seen from Fig. 13e,f that at the wind measurement points c and c1 behind the mountain, under the default turbulence coefficient, the maximum wind power density error is approximately 71% at distance of 3 m from the mountain surface, and the minimum wind power density error is approximately 56% at distance of 34 m from the mountain surface. Under the turbulence coefficient in the literature, the maximum wind power density error is approximately 68% at distance of 3 m from the mountain surface, and the minimum wind power density error is approximately 49% at distance of 34 m from the mountain surface. Under the corrected turbulence coefficient in this paper, the maximum wind power density error at distance of 3 m from the mountain surface is approximately 47%, and the minimum wind power density error at distance of 34 m from the mountain surface is approximately 39%.

Based on the comparative analysis of Fig. 13, it can be known that the error in front of the mountain < the error at the top of the mountain < the error behind the mountain. The error behind the mountain is the largest, which is caused by excessive turbulence behind the mountain due to fluid disturbance. However, the calculation errors at different elevations of the same plane position decrease with the increase of height, and the error trend is isotropic.

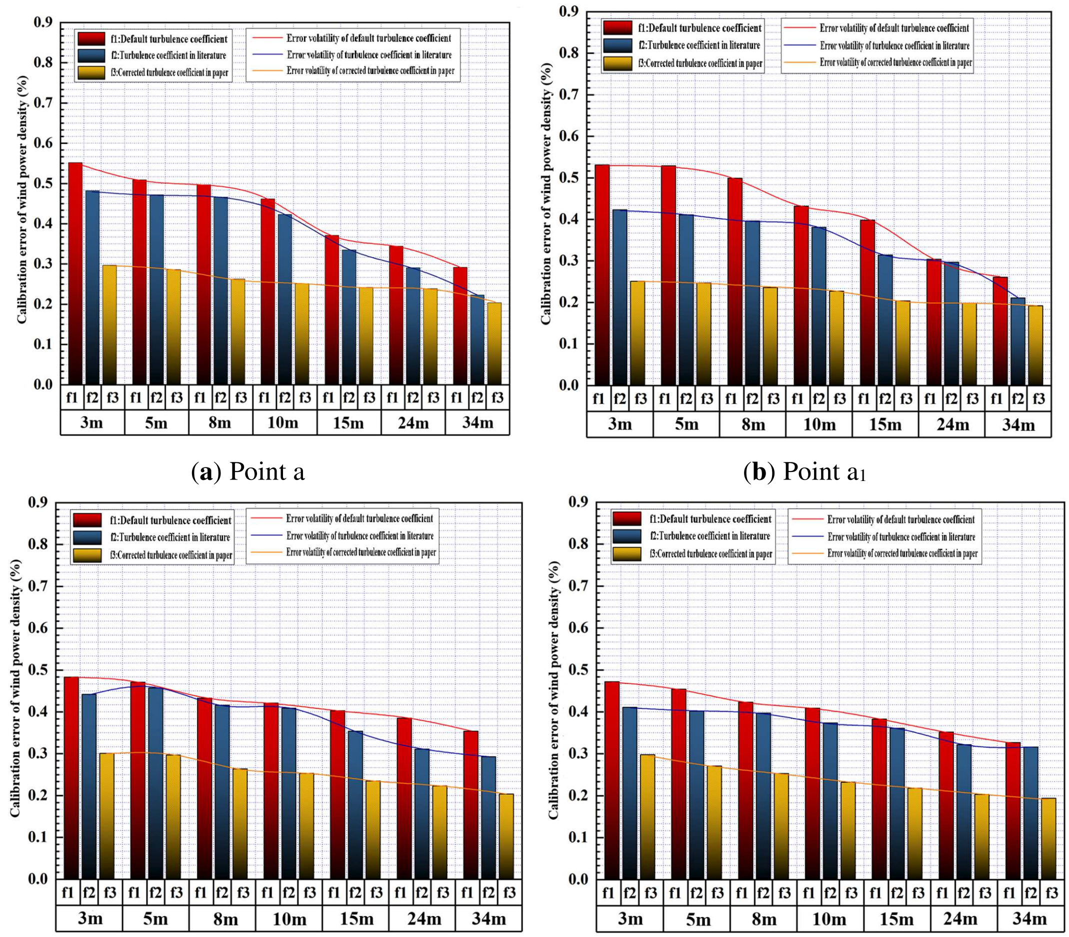

(**a**) Point a (**b**) Point a1

(**c**) Point b (**d**) Point b1

Figure 13: (Continued)

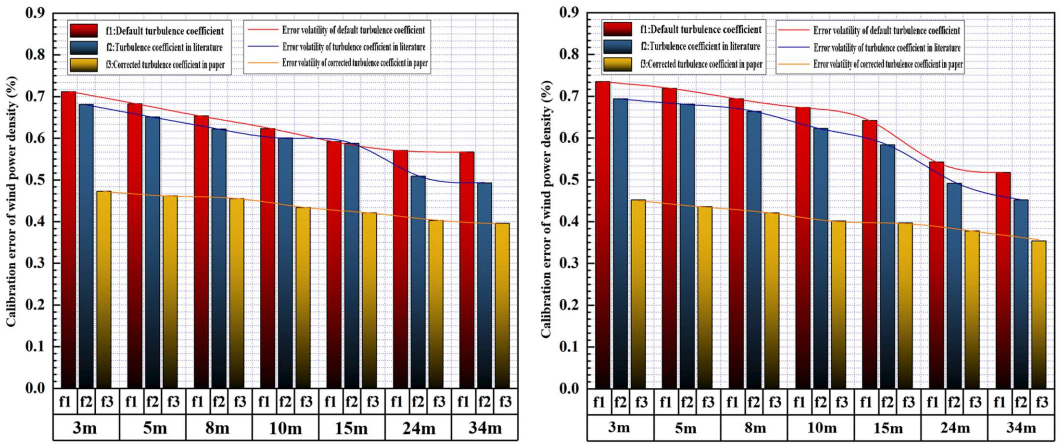

(**e**) Point c (**f**) Point c_1

Figure 13: Comparison chart of calibration errors of wind power density at different elevations

From the analysis of the above comparison results, it can be known that the numerical calibration of wind power density in complex terrain conditions is greatly affected by the terrain surface. The error magnitudes at different position points are different, and the error at different elevations of the same plane position decreases with the increase of height. The revised turbulence coefficient in this paper performs better than other coefficients in terms of error stability at different positions and elevations, and has higher reliability in the mutual inference of wind speed in actual wind resource assessment.

5 Conclusion

The numerical calibration of wind power in complex terrains is significantly influenced by topographical features. The error distribution varies spatially: the calculation error is minimized at the windward foot of the mountain and maximized in the leeward wake region. At a given horizontal location, the error diminishes with increasing altitude. Regarding grid strategies, while structured grids offer high accuracy in the free stream, they exhibit lower stability near complex terrain surfaces compared to unstructured grids. Therefore, a hybrid grid strategy—employing unstructured grids near the terrain surface and structured grids in the rest of the computational domain—is the optimal choice for engineering calculations.

Through computational analysis, the Richardson extrapolation method was proven effective in evaluating spatial discretization errors. Furthermore, the setting of the top boundary condition significantly impacts the simulation of the equilibrium atmospheric boundary layer. Results indicate that the velocity inlet condition is the optimal setting, followed by the symmetry boundary condition. Applying these boundary settings to actual complex terrains effectively improves the accuracy of numerical simulations.

Crucially, correcting the coefficients of the k-ε turbulence model is essential for complex terrain conditions. The optimized turbulence coefficients provide more stable numerical results in the calibration of power density values. This optimization strategy aligns with recent findings on improving CFD simulation accuracy in complex terrain, and effectively addresses the uncertainty factors in wind resource assessment highlighted in recent studies. However, it is important to note that the specific turbulence coefficients optimized in this study are based on the Askervein Hill benchmark. While these values are highly effective for similar complex terrains, applying them directly to significantly different topographies may carry an overfitting risk. Therefore, the core contribution of this work is the nonlinear orthogonal optimization methodology itself. In practical engineering applications, it is recommended to use this methodology to recalibrate turbulence parameters based on local field measurement data to ensure universal applicability.

Acknowledgement: We acknowledge the public availability of the Askervein Hill Project data, which served as the benchmark for this study.

Funding Statement: The authors received no specific funding for this study.

Author Contributions: Xin Guan conceived the study, designed the methodology, and conducted the experiments. Dechen Kong performed data analysis and visualization with support from Hao Tang. Bo Liu contributed the theoretical framework and supervised the computational modeling. Chuang Zhao drafted the manuscript, with critical revisions provided by all co-authors. The second to fifth authors are all affiliated with Shenyang Institute of Engineering. All authors reviewed the results and approved the final version of the manuscript.

Availability of Data and Materials: The Askervein Hill measurement data used to support the findings of this study are publicly available. The simulation data generated during the current study are available from the corresponding author on reasonable request.

Ethics Approval: This study does not involve human participants or animal experiments.

Conflicts of Interest: The authors declare no conflicts of interest.

References

1. Simão Ferreira C, Larsen GC, Sørensen JN. A theoretical upper limit for offshore wind energy extraction. Cell Rep Sustain. 2025;15:100573. doi:10.1016/j.crsus.2025.100573.
2. Fan W, Liu Y, Chappell A, Dong L, Xu R, Ekström M, et al. Evaluation of global reanalysis land surface wind speed trends to support wind energy development using *in situ* observations. J Appl Meteor Climatol. 2021;60(1):33–50. doi:10.1175/jamc-d-20-0037.1.
3. Manwell JF, McGowan JG, Rogers AL. Wind energy explained: theory, design and application. Hoboken, NJ, USA: John Wiley & Sons, Inc.; 2002. doi: 10.1002/0470846127.
4. Jung C, Schindler D. A review of recent studies on wind resource projections under climate change. Renew Sustain Energy Rev. 2022;165:112596. doi:10.1016/j.rser.2022.112596.
5. Vagiona DG, Tzekakis G, Loukogeorgaki E, Karanikolas N. Site selection of offshore solar farm deployment in the Aegean Sea, Greece. J Mar Sci Eng. 2022;10(2):224. doi:10.3390/jmse10020224.
6. Barber S, Schubiger A, Koller S, Eggli D, Radi A, Rumpf A, et al. The wide range of factors contributing to wind resource assessment accuracy in complex terrain. Wind Energ Sci. 2022;7(4):1503–25. doi:10.5194/wes-7-1503-2022.
7. Haupt SE, Kosović B, Berg LK, Kaul CM, Churchfield M, Mirocha J, et al. Lessons learned in coupling atmospheric models across scales for onshore and offshore wind energy. Wind Energ Sci. 2023;8(8):1251–75. doi:10.5194/wes-8-1251-2023.
8. Song JL, Li JW, Xu RZ, Flay RGJ. Field measurements and CFD simulations of wind characteristics at the Yellow River bridge site in a converging-channel terrain. Eng Appl Comput Fluid Mech. 2022;16(1):58–72. doi:10.1080/19942060.2021.2004240.
9. Zou Y, Yue P, Liu Q, He X, Wang Z. Wind field characteristics of complex terrain based on experimental and numerical investigation. Appl Sci. 2022;12(10):5124. doi:10.3390/app12105124.
10. Yoon M. Direct numerical simulation of turbulent boundary layer over cubical roughness elements. Appl Sci. 2024;14(4):1418. doi:10.3390/app14041418.
11. Song JL, Li JW, Flay RGJ, Ali Safaei Pirooz A, Fu JY. Validation and application of pressure-driven RANS approach for wind parameter predictions in mountainous terrain. J Wind Eng Ind Aerodyn. 2023;240(9–11):105483. doi:10.1016/j.jweia.2023.105483.

12. Ayuso-Virgili G, Christakos K, Lande-Sudall D, Lümmen N. Measure-correlate-predict methods to improve the assessment of wind and wave energy availability at a semi-exposed coastal area. Energy. 2024;309:132904. doi:10.1016/j.energy.2024.132904.
13. Shen L, Han Y, Cai CS, Hu P, Lei X, Zhou P, et al. Equilibrium atmospheric boundary layer model for numerical simulation of urban wind environment. Phys Fluids. 2024;36(8):085177. doi:10.1063/5.0216503.
14. Ma G, Tian L, Song Y, Zhao N. Effects of turbulence modeling on the simulation of wind flow over typical complex terrains. Appl Sci. 2024;14(23):11438. doi:10.3390/app142311438.
15. Bretos D, Campaña-Alonso G, Méndez-López B, Cantero-Nouqueret E. CFD wind farm evaluation in complex terrain under free and wake induced flow conditions. J Phys. 2024;2767(9):092099. doi:10.1088/1742-6596/2767/9/092099.
16. He JY, Li QS, Chan PW, Li L, Lu C, Zhang L, et al. Characteristics and vertical profiles of mean wind and turbulence for typhoon, monsoon, and thunderstorm winds. J Struct Eng. 2021;147(11):04021188. doi:10.1061/(asce)st.1943-541x.0003156.
17. Fritts DC, Baumgarten G, Pautet PD, Hecht JH, Williams BP, Kaifler N, et al. Kelvin-Helmholtz instability "tube" and "knot" dynamics. Part I: expanding observational evidence of occurrence and environmental influences. J Atmos Sci. 2023;80(10):2419–37. doi:10.1175/jas-d-22-0189.1.
18. Wani AH, Varma RK. Comparative wind tunnel analysis of wind flow characteristics over gentle and steep escarpment slopes. Civ Eng Infrastruct J. 2025:1–21. doi:10.22059/ceij.2025.389658.2242.
19. Lv ZF. Research on the influence of complex mountainous terrain on wind speed distribution in wind farms [dissertation]. Kunming, China: Kunming University of Science and Technology; 2015. (In Chinese).
20. Wang W, Chen F. Wind field modeling over hilly terrain: a review of methods, challenges, limitations, and future directions. Appl Sci. 2025;15(18):10186. doi:10.3390/app151810186.
21. Sharma A, Brazell MJ, Vijayakumar G, Ananthan S, Cheung L, DeVelder N, et al. ExaWind: open-source CFD for hybrid-RANS/LES geometry-resolved wind turbine simulations in atmospheric flows. Wind Energy. 2024;27(3):225–57. doi:10.1002/we.2886.
22. Sabatini MH, Pinto MAV, Martins MA, de Oliveira ML, Rodrigues S. Reduction and estimation of discretization error using repeated Richardson extrapolation: a study involving two-phase flow problems in porous media. Numer Heat Transf Part B Fundam. 2025:1–19. doi:10.1080/10407790.2025.2530192.
23. Barile DA, Sosa R, Aubrun S, Otero AD. Novel CFD approach for simulation of an ABL wind tunnel flow: validation and application to a FOWT model. Wind Energy Sci Discuss. 2025;2025:1–20. doi:10.5194/wes-2025-2.
24. Yamaguchi A, Tavana A, Ishihara T. Assessment of wind over complex terrain considering the effects of topography, atmospheric stability and turbine wakes. Atmosphere. 2024;15(6):723. doi:10.3390/atmos15060723.
25. Esgandari B, Schneiderbauer S. On grid-independency of CFD-DEM simulations of cluster-induced turbulence. Int J Multiph Flow. 2025;188(2):105223. doi:10.1016/j.ijmultiphaseflow.2025.105223.
26. Tao L, Zhang F, Sun P, Li X. Optimization of k-ε RNG turbulence model parameters using genetic algorithm for enhanced wind field simulation in complex mountainous terrain. J Phys. 2025;3078(1):012064. doi:10.1088/1742-6596/3078/1/012064.
27. Cheng L, Yin L. Editorial: impacts of complex terrain on wind power output and mechanisms to improve prediction accuracy. Front Energy Res. 2024;12:1468799. doi:10.3389/fenrg.2024.1468799.